

Polarization dependent nanostructuring of silicon with femtosecond vortex pulse

M. G. Rahimian, F. Bouchard, H. Al-Khazraji, E. Karimi, P. B. Corkum, and V. R. Bhardwaj^a

Department of Physics, Advanced Research Complex, University of Ottawa, 25 Templeton Street, Ottawa, Ontario K1N 6N5, Canada

(Received 10 April 2017; accepted 6 August 2017; published online 24 August 2017)

We fabricated conical nanostructures on silicon with a tip dimension of ~ 70 nm using a single twisted femtosecond light pulse carrying orbital angular momentum ($\ell = \pm 1$). The height of the nano-cone, encircled by a smooth rim, increased from ~ 350 nm to ~ 1 μm with the pulse energy and number of pulses, whereas the apex angle remained constant. The nano-cone height was independent of the helicity of the twisted light; however, it is reduced for linear polarization compared to circular at higher pulse energies. Fluid dynamics simulations show nano-cones formation when compressive forces arising from the radial inward motion of the molten material push it perpendicular to the surface and undergo re-solidification. Simultaneously, the radial outward motion of the molten material re-solidifies after reaching the cold boundary to form a rim. Overlapping of two irradiated spots conforms to the fluid dynamics model. © 2017 Author(s). All article content, except where otherwise noted, is licensed under a Creative Commons Attribution (CC BY) license (<http://creativecommons.org/licenses/by/4.0/>). [<http://dx.doi.org/10.1063/1.4999219>]

Light-matter interaction can be controlled by manipulating the beam polarization, spatial intensity, and phase profile. Structured light in the form of non-conventional beam shapes, such as Bessel, Airy, Laguerre-Gaussian, or optical vortex (OV) beams has been used in optical trapping and manipulation,^{1,2} atom guiding,^{3,4} and super resolution microscopy.^{5,6} Recently, structured light has been extended to material processing,⁷⁻⁹ specifically OV beams.^{10,11,13-19} Optical vortices in the form of helical beams have an annular intensity profile with an orbital angular momentum $\ell\hbar$ per photon, where ℓ indicates the number of twists in the helical wavefront in one wavelength and its sign determines the chirality of the helix. They can also possess spin angular momentum $s\hbar$ per photon associated with polarization helicity with values of $s = \pm 1$ corresponding to the left and right circular polarizations. OV beams are produced from a fundamental Gaussian mode using holograms,²⁰ cylindrical lenses,²¹ spiral phase plates,^{22,23} S-waveplates,²⁴ and q -plates.²⁵⁻²⁸

Material processing with a single nano- and pico-second OV pulse produced micro-needles^{10,11,16-18} that exhibited spiral conical structures with the handedness of the optical vortex pulse imprinted on them. Their growth was controlled with the number of pulses. In contrast, micro-needle/nanopillar formation with a single femtosecond OV pulse remains ambiguous. Annular ablation craters with no features in the centre were produced by loosely focusing the OV pulse.^{7,11} However, tight focusing produced a nanopillar that disappeared when (a) the polarization was switched from radial to azimuthal and (b) a second radially polarized pulse was incident on the sample.¹² In multi-pulse ablation, complex periodic surface patterns were fabricated using femtosecond OV beams with different spatial distributions of the state of polarization.^{9,13-15} However, the role of laser polarization remains unclear in nano-cone formation with a single laser OV pulse.

In this paper, we demonstrate polarization dependent nano-cone formation with a single femtosecond OV pulse with $\ell = \pm 1$. By manipulating the spatial profile of the laser beam, we show that irradiation of silicon with a single femtosecond Gaussian pulse formed a rim around the ablation

^aElectronic mail: ravi.bhardwaj@uottawa.ca

crater while an OV pulse formed a nano-cone encircled by a rim, irrespective of laser polarization. We simulate the action of the laser pulse on fluid dynamics of the molten silicon and show that the radial inward (outward) motion of the molten silicon forms the nano-cone (rim). We demonstrate the nano-cone height to decrease at higher pulse energies for linear compared to that of circular polarization. This behaviour was attributed to an asymmetry in the radial inward fluid motion that arises from transient light-plasma interaction.

Linearly polarized light from a Ti:Sapphire laser (operating at 1 kHz repetition rate and producing 800 nm, 45 fs pulses) was transformed into the left- or right-circularly polarized beam ($s = \pm 1$) by a quarter-wave plate (QWP). A q -plate with a topological charge of $q = 1/2$ produced OV beams with $\ell = \pm 1$ and inverted polarization ($s = \mp 1$).²⁶ A linearly polarized OV beam ($s = 0, \ell = \pm 1$) was produced by a second QWP and a polarizer. Electrically detuning the q -plate generated Gaussian beams. A 0.25 NA (16 \times) aspheric objective focused the femtosecond pulse onto a p-type silicon surface [(100) orientation] mounted on a three-axis translation stage.

For a Gaussian beam, the focal spot size was measured to be $1.8 \pm 0.1 \mu\text{m}$ using the knife-edge method. For an OV beam, the spot size, defined as the diameter of the maximum intensity, was measured to be $2.8 \pm 0.2 \mu\text{m}$ compared to a theoretical value of $2.3 \mu\text{m}$.²⁹ The ablated regions were characterized by a scanning electron microscope (SEM) with the electron beam perpendicular to the sample (zero tilt) and at an angle of 88° and by an atomic force microscope (AFM) in non-contact mode.

Figure 1 shows SEM [(a) and (b)] and the corresponding 3D AFM profiles [(c) and (d)] of micro-structures on silicon induced by single, circularly polarized, femtosecond Gaussian, and

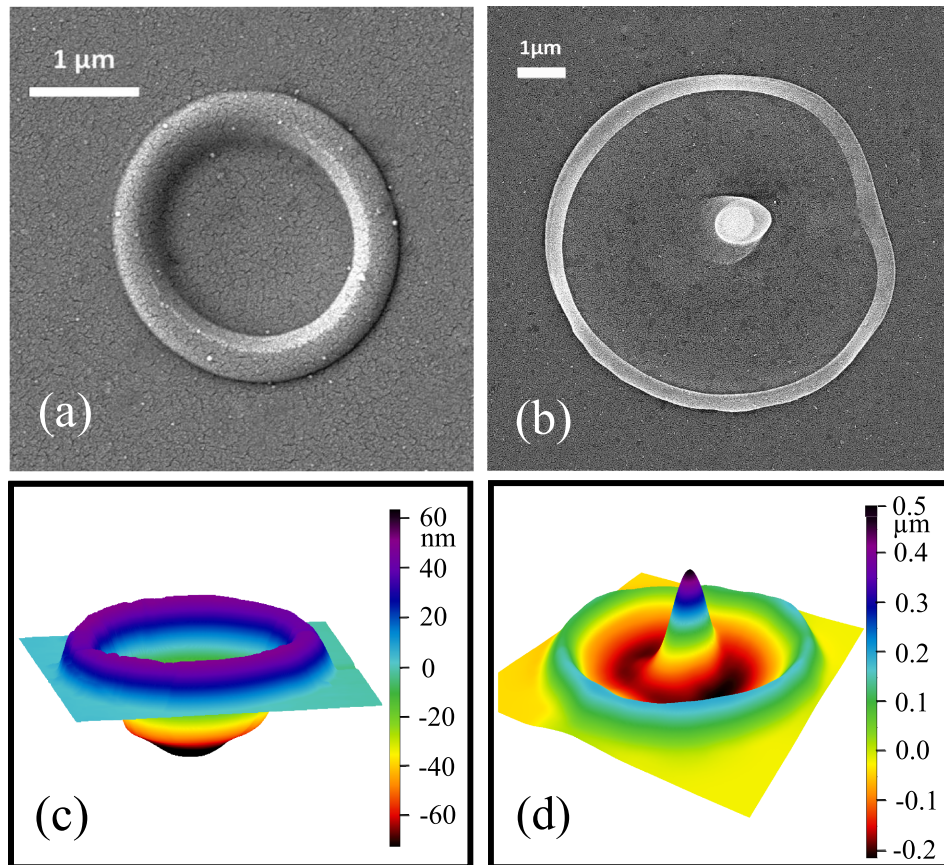


FIG. 1. SEM [(a) and (b)] and AFM [(c) and (d)] images of surface topography induced by a single femtosecond laser pulse in p-type silicon [(100) orientation] with circularly polarized Gaussian and vortex beams ($\ell = -1, s = +1$) with pulse energies of 150 nJ and 310 nJ, respectively.

OV pulses ($\ell = -1, s = +1$), respectively. The Gaussian pulse produced a rim with a uniform height of ~ 50 nm around a ~ 70 nm deep ablation crater. Besides the rim, the OV pulse also produced a nano-cone in the middle of the ablation crater protruding ~ 450 nm above the surface. Similar structures were observed for intrinsic and n-type silicon. The single shot ablation threshold of silicon, defined as the lowest energy at which ablation features were visible under SEM, was determined to be 55 nJ (19 nJ) for an OV (Gaussian) beam corresponding to peak laser fluence of 0.41 J/cm² (0.37 J/cm²), in good agreement with the published data.^{13,30–32} A small asymmetry in the rim shape was due to a slight misalignment of the beam through the q -plate.

Evolution of the ablation crater features with pulse energy for a single femtosecond vortex pulse is shown in Fig. 2. Four key observations can be made.

First, the nano-cone height was independent of the handedness of the twisted light ($\ell = \pm 1$) with spin ($s = \mp 1$), corresponding to a total angular momentum, $j = \ell + s = 0$. Formation of a nano-cone with a single femtosecond OV pulse differs from previous reports in three aspects. (i) Only pico- and nano-second pulses produced micro-needles,¹¹ while femtosecond pulses produced annular ablation craters with no features in the centre. (ii) Ablation with a single twisted nanosecond OV pulse with $j = 0$ produced no central protuberance.¹⁸ It required overlapping of several twisted light pulses to produce a nanostructure. (iii) The tightly focused circularly polarized femtosecond vortex pulse ablated the material differently depending on the polarization handedness of light.³³

Second, the nano-cone height increased with pulse energy at two different rates: ~ 0.6 nm/nJ and 0.2 nm/nJ below and above 600 nJ, respectively, for left- and right-circular polarizations ($j = 0$).

Third, the nano-cone height increased at the same rate for linear ($j = +1$) and circular ($j = 0$) polarizations up to 600 nJ. Beyond this energy, the nano-cone height decreased for linear polarization at a rate of ~ 1.3 nm/nJ (highlighted by an ellipse). This is discussed below in terms of an asymmetry in compressive forces that causes nano-cone formation.

Fourth, rim height and crater depth increased with pulse energy at the same rate for all three polarizations.

Figure 3 shows variation of the nano-cone width, measured at the surface, and the apex angle with pulse energy. The nano-cone width varied from 1.4 μm to 1.9 μm with two different rates

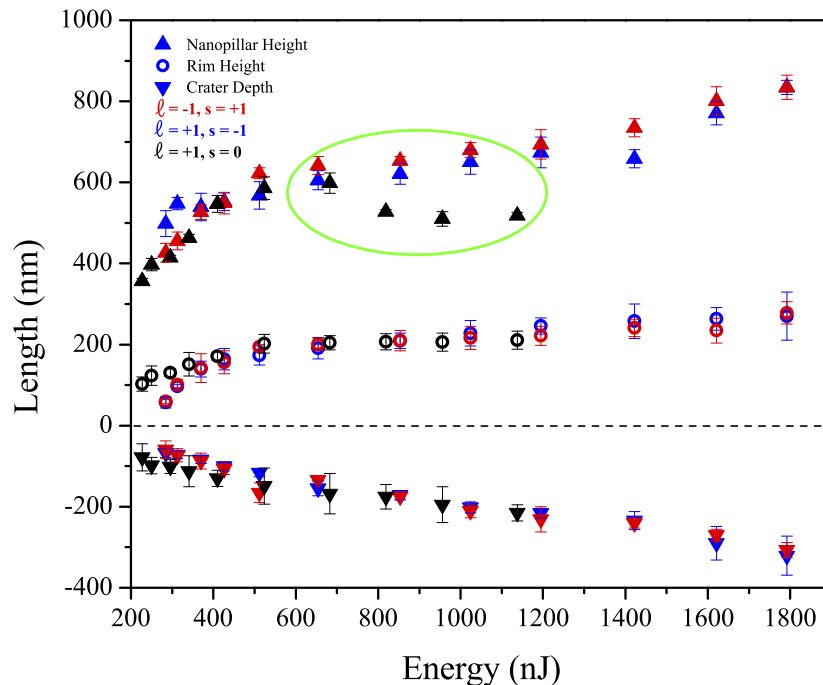


FIG. 2. Nano-cone height (Δ), rim height (\circ), and crater depth (∇) relative to the sample surface as a function of pulse energy for three different cases: (i) $\ell = -1, s = +1$ (red), (ii) $\ell = +1, s = -1$ (blue), and (iii) $\ell = +1, s = 0$ (black). In all cases, a single femtosecond OV pulse irradiated the sample.

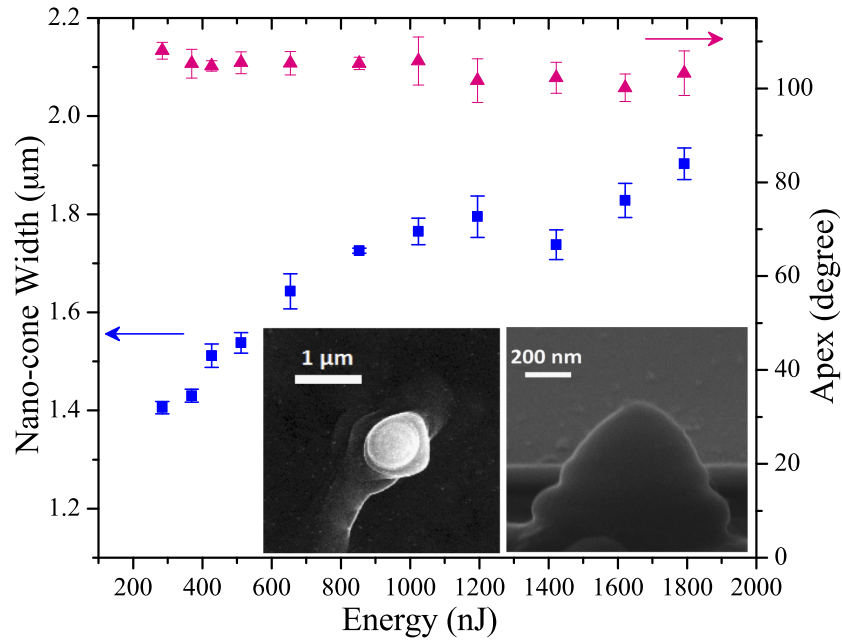


FIG. 3. Nano-cone width (left axis) and the apex angle (right axis) as a function of pulse energy for a single femtosecond OV pulse ($\ell = +1$, $s = -1$). The insets show SEM images of a nano-cone at a pulse energy of 370 nJ; top view (left panel) and side view at a tilt angle of 88° (right panel).

-0.6 nm/nJ (0.18 nm/nJ) below (above) 700 nJ, similar to the height. However, the apex angle (measured with an AFM and SEM) remained nearly constant at 105° , decreasing marginally at higher energies. The radius of curvature of the nano-cone was about 70 nm. The insets show SEM images of the nano-cone at a pulse energy of 370 nJ. While the top view (left panel) suggests a spiral conical structure, it could not be confirmed by the side view (right panel) even when the handedness of the twisted light was changed. In contrast, spiral needles of several microns in length were produced with

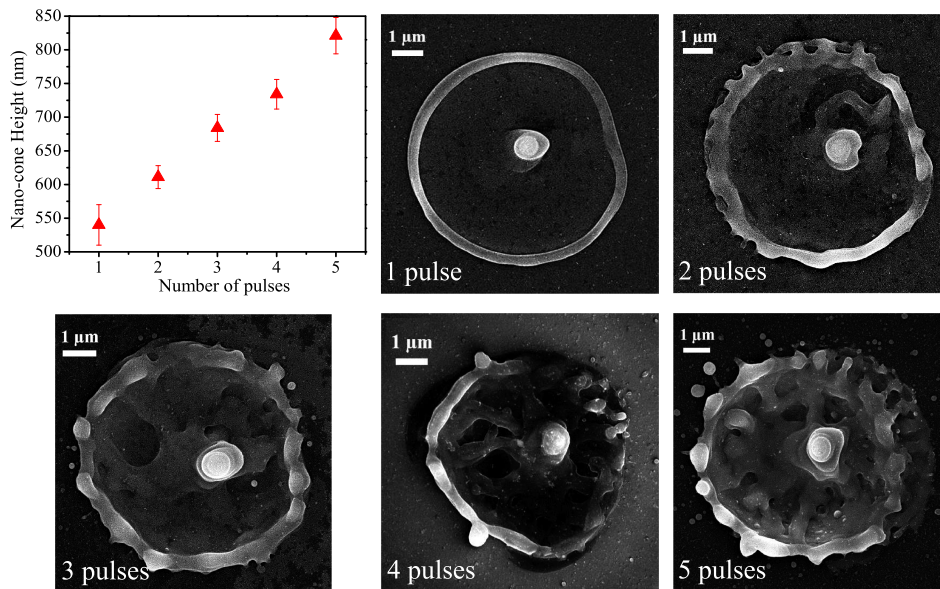


FIG. 4. Nano-cone height for different number of laser pulses for a fixed energy of 310 nJ ($\ell = -1$, $s = +1$). Also shown are SEM images.

pico- and nano-second pulses.^{11,17,18} This could be due to significantly lower height of the nano-cone and shorter duration of the OV pulse, thereby obscuring the effects of the twisted light.

The height of the nano-cone induced by the OV pulse of fixed energy increased with the number of laser pulses as shown in Fig. 4. However, the aspect ratio, defined as the ratio of the height of the nano-cone to its width, varied marginally from ~ 0.38 for a single pulse to ~ 0.45 for 5 pulses. This was in contrast to the narrowing of the micro-needle observed with nanosecond light pulses.¹⁸ SEM images show that with increased number of laser pulses, more molten material was pushed to the outer rim forming nano droplets. Also, the inside of the ablation crater developed ripples.

Polarization dependent rim formation on silicon irradiated by a single femtosecond Gaussian pulse has been recently observed³⁴⁻³⁶ and discussed in terms of fluid dynamics³⁴ which can be

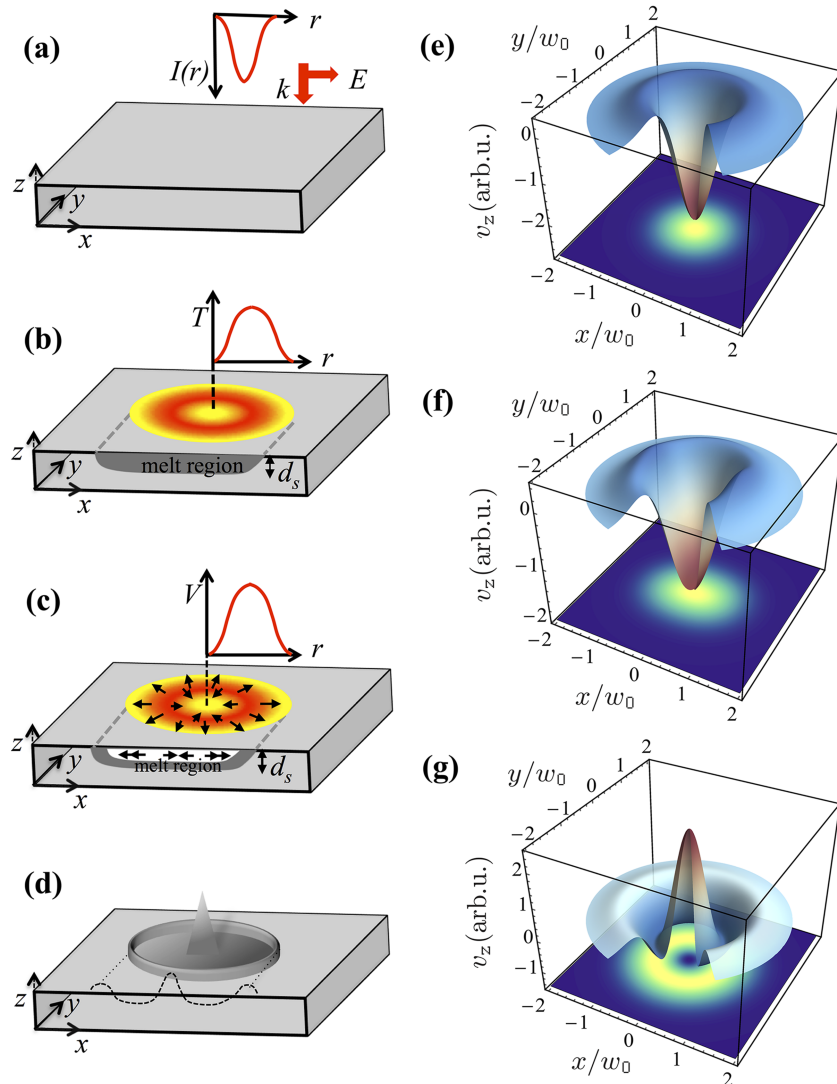


FIG. 5. (a)–(d) Schematic showing rim and nano-cone formation with an OV beam at different stages of the interaction. (a) Intensity distribution of the incident pulse. k and E are propagation and polarization directions, respectively. (b) Spatial profile of the temperature distribution d_s is the melt layer thickness. (c) Displacement of molten silicon indicated by arrows and melt layer velocity profile due to the exerted forces. (d) Nano-cone (rim) formation by radial inward (outward) motion of molten silicon. (e)–(g) Mass transport $v_z(r, \phi)$ for several temperature distributions (shown at the bottom) given by (e) symmetric Gaussian profile, (f) an asymmetric Gaussian profile, and (g) a symmetric Laguerre-Gaussian profile with a mode index of $\ell = 1$ and $p = 0$. The asymmetry in (f) was obtained by multiplying the Gaussian distribution by $(1 + y^2)$, where we consider the first order symmetric distortion.

extended to the vortex pulse. The annular intensity distribution of the OV beam is mapped onto the spatial profile of the free carriers generated by linear and two-photon absorption [Fig. 5(a)]. Picoseconds later, when energy of the free carriers is transferred to the lattice, the temperature distribution retains the shape of OV beam intensity distribution [Fig. 5(b)]. When melting occurs on nanoseconds, only a thin layer of molten silicon is formed, determined by the skin depth d_s . Thermocapillary^{37–39} and/or hydrodynamic forces⁴⁰ displace the molten silicon radially outward to the periphery and also radially inward to the centre of the crater [Fig. 5(c)]. The outward motion leads to rim formation similar to a Gaussian beam. The inward motion leads to a compressive force that pushes the molten material away from the surface. Rapid expansion causes resolidification into a nano-cone [Fig. 5(d)]. The temporal evolution of the silicon micro-needle formation was recently captured with an ultra-high speed camera.¹¹

To gain further insight, we simulated the action of the short laser pulse on the fluid dynamics of the molten silicon. We solved the continuity and Navier-Stokes equations using the methodology of Schwarz-Selinger *et al.*³⁷ under the assumption of incompressibility, large viscosity, and steady-state flow. To simulate the effect of laser polarization with an asymmetric distribution, we have generalized the calculation to the full two-dimensional transverse coordinate (r and ϕ or x and y) and extended it to include Laguerre-Gaussian intensity profile. The boundary conditions are such that the fluid velocity must vanish at the bottom of the molten material and that the fluid velocity at the surface is given in relation to the surface tension, i.e., $\mathbf{v} = 0$ at $z = -h$; $\eta (\partial_z v_r + \partial_r v_z) = \partial_r \alpha$ at $z = 0$; $\eta (\partial_z v_\phi + r^{-1} \partial_\phi v_z) = r^{-1} \partial_\phi \alpha$ at $z = 0$. Here, η is the dynamic viscosity of the fluid, α is the surface tension, and r , ϕ , and z are the cylindrical coordinates.

Radial velocity and azimuthal velocity (v_r and v_ϕ) were obtained by solving the Navier-Stokes equation. Substituting them in the continuity equation and integrating with respect to z gives $v_z = (2\eta r)^{-1} (\partial_r (h^2 \partial_r \alpha) + \partial_\phi (h^2 \partial_\phi \alpha))$. For the case in which the melt depth is independent of the transverse coordinates, r and ϕ , the above expression takes the simple form of, $v_z(r, \phi) = \frac{h^2}{2\eta} \nabla_\perp^2 \alpha$, where $\nabla_\perp^2 := r^{-1} \partial_r (r \partial_r) + r^{-2} \partial_\phi \partial_\phi$ is the transverse Laplacian operator. For simple materials, the surface tension may be given in terms of the temperature at the surface, where $\partial_T \alpha$ is often constant (independent of the temperature). Since the temperature distribution is proportional to the intensity profile of the incoming short pulse, i.e., $T(r, \phi) \propto I(r, \phi)$, the mass transport in the fluid can be approximated by $v_z(r, \phi) \propto \nabla_\perp^2 I$.

To calculate the mass transport for various intensity distributions of the laser pulse, we used Laguerre-Gaussian beams given by the following intensity profiles, $I(\rho) = A \rho^{2|\ell|} L_p^{|\ell|} (2\rho^2) \exp(-2\rho^2)$. Here, A is a constant that depends on the power of the laser pulse, $L_p^{|\ell|}(\cdot)$ are the associated Laguerre polynomials, ℓ and p are the azimuthal and radial mode indices, respectively, $\rho = r/w_0$, and w_0 is the beam waist at the focus.

Figure 5(e) shows the mass transport for a Gaussian beam with the temperature distribution shown at the bottom. The longitudinal velocity, $v_z(r, \phi)$, is maximum at the centre of the interaction region pointing towards the thin layer of molten silicon. The resultant displacement causes the molten material to accumulate at the edges where $v_z(r, \phi)$ is pointing away from the silicon surface. This fluid motion leads to formation of a rim around the ablation crater.

When an asymmetry was introduced in the temperature distribution along a given direction, it is reflected in the mass transport giving rise to an asymmetric rim height and width as shown in Fig. 5(f). Such an asymmetry was observed for linearly polarized light, whereas it did not exist for circular polarization.³⁴ The polarization dependence was explained in terms of transient plasmonics.^{41,42} A dense free carrier plasma is created by the leading edge of an intense femtosecond pulse. The trailing edge of the pulse then interacts with the plasma giving rise to local field enhancement. The resultant asymmetry in the carrier distribution eventually translates into an asymmetric distribution of lattice temperature and hence thermocapillary/hydrodynamics forces. The field enhancement occurs along or perpendicular to the laser polarization depending on the plasma density.⁴²

For an OV beam, the annular intensity profile translates into a doughnut shaped temperature distribution as shown in Fig. 5(g). Where temperature is maximum, mass transport points towards the molten silicon. However, $v_z(r, \phi)$ is maximum at the centre, pointing away from the silicon surface.

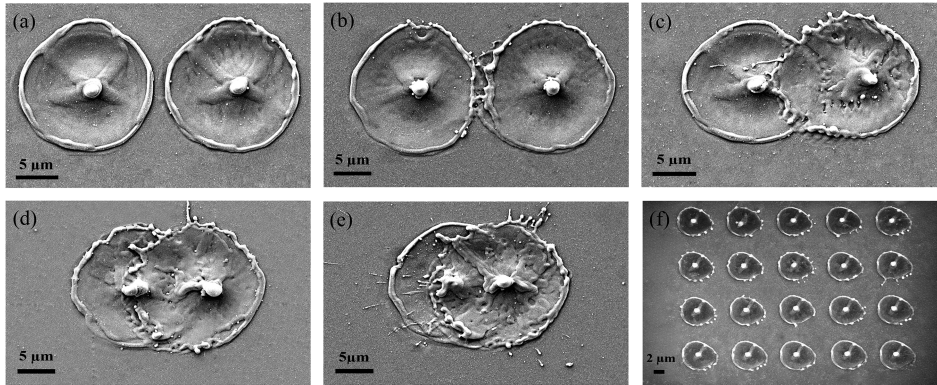


FIG. 6. (a)–(e) SEM images of two overlapping structures with successive irradiation of silicon with a single femtosecond OV pulse ($\ell = +1$, $s = -1$) with a separation of $16 \mu\text{m}$, $15 \mu\text{m}$, $10 \mu\text{m}$, $7 \mu\text{m}$, and $5 \mu\text{m}$, respectively. (f) SEM image of a 5×4 array of nano-cones. The pulse energy was 850 nJ .

The resultant displacement causes molten silicon to move radially both outward and inwards forming the rim and nano-cone, respectively.

We now address the decrease in nano-cone height at higher pulse energies for the linearly polarized vortex pulse, shown in Fig. 2. Local field enhancement resulting from light-plasma interaction leads to an asymmetry in the radial inward motion of the molten material. The resultant asymmetric compressive force causes the nano-cone height to be less. The local field enhancement *vis-a-vis* asymmetric compressive force becomes prominent at higher pulse energies. As a result, the height of the nano-cone with linear polarization deviates from that of a circularly polarized vortex pulse.

The role of fluid dynamics in the nano-cone formation is evident from SEM images of Fig. 6. Silicon was irradiated with a single vortex pulse at two different spots. At $16 \mu\text{m}$ separation [Fig. 6(a)], the ablation crater morphology was unaffected by the presence of the other. At $15 \mu\text{m}$ spacing, molten silicon from the second spot collided with the resolidified rim of the first spot deforming the rim at the point of contact [Fig. 6(b)]. When the two spots overlapped ($10 \mu\text{m}$ separation), the nano-cones remained unaffected, but the rim of the first spot vanished in the overlap region [Fig. 6(c)]. When the spacing was reduced further, the molten material was propelled past the first nano-cone [Fig. 6(d)] and eventually disrupted it [Fig. 6(e)]. Intactness of the nano-cones even when the irradiated spots overlapped enables one to fabricate arrays of silicon nano-cones similar to those shown in Fig. 6(f).

To conclude, we demonstrated fabrication of a nano-cone on silicon with a single femtosecond OV pulse. Its formation was described in terms of fluid dynamics, and its polarization dependence was attributed to transient light-plasma interaction. Our results highlight key aspects of light-matter interaction. First, the fluid dynamics model suggests that any tightly focussed annular beam will produce a nano-cone. Tighter focusing by higher numerical aperture objectives can lead to higher compressive forces and can further increase the height of the nano-cone. Second, transient plasmonics influences the laser processed structures. Intense linearly polarized femtosecond light pulses distort the free-carrier density distribution due to local field effects that is imprinted on the subsequent steps of the ablation/modification process.^{34,41,43} Its effects can be minimized by using circularly polarized light.

One potential application of the laser fabricated nano-cone arrays in silicon is to enhance high harmonic radiation that has recently been demonstrated in bulk materials.^{44–47} For example, an array of nano-antennas was used to show enhancement of plasmon assisted high harmonic generation from crystalline silicon substrate.⁴⁸ Also, nanostructured ZnO and silicon were used to demonstrate customized high-harmonic wave fields and to confine them to diffraction-limited spot sizes.⁴⁹ Structured light enables to not only alter the surface topography of a target material and possibly change its phase but also investigate the target by generating high harmonics. This all-optical technique can provide an opportunity to control and probe light-induced dynamical changes to material properties.

The authors acknowledge financial support from Natural Science and Engineering Research Council of Canada, Canada Research Chairs, Canadian Foundation for Innovation and Ontario Ministry of Economic Development and Innovation.

- ¹ V. Garcés-Chavez, D. McGloin, H. Melville, W. Sibbett, and K. Dholakia, *Nature* **419**, 145 (2002).
- ² V. G. Shvedov, A. V. Rode, Y. V. Izdebskaya, A. S. Desyatnikov, W. Krolikowski, and Y. S. Kivshar, *Phys. Rev. Lett.* **105**, 118103 (2010).
- ³ M. Padgett, J. Courtial, and L. Allen, *Phys. Today* **57**(5), 35 (2004).
- ⁴ M. Mazilu, D. Stevenson, F. Gunn-Moore, and K. Dholakia, *Laser Photonics Rev.* **4**, 529 (2010).
- ⁵ S. W. Hell and J. Wichmann, *Opt. Lett.* **19**, 780 (1994).
- ⁶ S. W. Hell, *Nat. Methods* **6**, 24 (2009).
- ⁷ C. Hnatovsky, V. G. Shvedov, W. Krolikowski, and A. V. Rode, *Opt. Lett.* **35**, 3417 (2010).
- ⁸ C. Hnatovsky, V. G. Shvedov, W. Krolikowski, and A. V. Rode, *Phys. Rev. Lett.* **106**, 123901 (2010).
- ⁹ K. Lou, S. X. Qian, X. L. Wang, Y. Li, B. Gu, C. Tu, and H. T. Wang, *Opt. Express* **20**, 120 (2012).
- ¹⁰ F. Takahashi, S. Takizawa, H. Hidai, K. Miyamoto, R. Morita, and T. Omatsu, *Phys. Status Solidi A* **213**, 1063 (2016).
- ¹¹ F. Takahashi, K. Miyamoto, H. Hidai, K. Yamane, R. Morita, and T. Omatsu, *Sci. Rep.* **6**, 21738 (2016).
- ¹² R. Drevinskas, J. Zhang, M. Beresna, M. Gecevičius, A. G. Kazanskii, Y. P. Svirko, and P. G. Kazansky, *Appl. Phys. Lett.* **108**, 221107 (2016).
- ¹³ J. J. J. Nivas, H. Shutong, K. K. Anoop, A. Rubano, R. Fittipaldi, A. Vecchione, D. Paparo, L. Marrucci, R. Bruzzese, and S. Amoruso, *Opt. Lett.* **40**, 4611 (2015).
- ¹⁴ K. K. Anoop, R. Fittipaldi, A. Rubano, X. Wang, D. Paparo, A. Vecchione, L. Marrucci, R. Bruzzese, and S. Amoruso, *J. Appl. Phys.* **116**, 113102 (2014).
- ¹⁵ J. J. J. Nivas, H. Shutong, A. Rubano, A. Vecchione, D. Paparo, L. Marrucci, R. Bruzzese, and S. Amoruso, *Sci. Rep.* **7**, 42142 (2017).
- ¹⁶ K. Toyoda, F. Takahashi, S. Takizawa, K. Miyamoto, R. Morita, and T. Omatsu, *Phys. Rev. Lett.* **110**, 143603 (2013).
- ¹⁷ K. Toyoda, K. Miyamoto, M. Aoki, R. Morita, and T. Omatsu, *Nano Lett.* **12**, 3645 (2012).
- ¹⁸ T. Omatsu, K. Chujo, K. Miyamoto, M. Okida, K. Nakamura, N. Aoki, and R. Morita, *Opt. Express* **18**, 17967 (2010).
- ¹⁹ S. Syubaev, A. Zhizhchenko, A. Kuchmizhak, A. Porfirev, E. Pustovalov, O. Vitrik, Yu. Kulchin, S. Khonina, and S. Kudryashov, *Opt. Express* **25**, 10214 (2017).
- ²⁰ V. Y. Bazhenov, M. V. Vlasov, and M. S. Soskin, *J. Exp. Theor. Phys. Lett.* **52**, 429 (1990).
- ²¹ L. Allen, N. W. Beijersbergen, R. J. C. Spreeuw, and J. P. Woerdman, *Phys. Rev. A* **45**, 8185 (1992).
- ²² M. W. Beijersbergen, R. P. C. Coerwinkel, M. Kristensen, and J. P. Woerdman, *Opt. Commun.* **112**, 321 (1994).
- ²³ K. Sueda, G. Miyaji, N. Miyana, and M. Nakatsuka, *Opt. Express* **12**, 3548 (2004).
- ²⁴ M. Beresna, M. Gecevičius, P. G. Kazansky, and T. Gertus, *Appl. Phys. Lett.* **98**, 201101 (2011).
- ²⁵ E. Karimi, B. Piccirillo, E. Nagali, L. Marrucci, and E. Santamato, *Appl. Phys. Lett.* **94**, 231124 (2009).
- ²⁶ L. Marrucci, E. Karimi, S. Slussarenko, B. Piccirillo, E. Santamato, E. Nagali, and F. Sciarrino, *J. Opt.* **13**, 064001 (2011).
- ²⁷ S. Slussarenko, A. Murauski, T. Du, V. Chigrinov, L. Marrucci, and E. Santamato, *Opt. Express* **19**, 4085 (2011).
- ²⁸ H. Larocque, J. Gagnon-Bischoff, F. Bouchard, R. Fickler, J. Upham, R. W. Boyd, and E. Karimi, *J. Opt.* **18**, 124002 (2016).
- ²⁹ F. Bouchard, J. Harris, H. Mand, R. W. Boyd, and E. Karimi, *Optica* **3**, 351 (2016).
- ³⁰ J. Bonse, S. Baudeach, J. Kruger, W. Kautek, and M. Lenzner, *Appl. Phys. A* **74**, 19 (2002).
- ³¹ A. Borowiec, M. Mackenzie, G. C. Weatherly, and H. K. Haugen, *Appl. Phys. A* **76**, 201 (2003).
- ³² J. Bonse, K.-W. Brzezinka, and A. J. Meixner, *Appl. Surf. Sci.* **221**, 215 (2004).
- ³³ C. Hnatovsky, V. G. Shvedov, N. Shostka, A. V. Rode, and W. Krolikowski, *Opt. Lett.* **37**, 226 (2012).
- ³⁴ H. Al-Khazraji and V. R. Bhardwaj, *Appl. Surf. Sci.* **353**, 600 (2015).
- ³⁵ J. Zhang, R. Drevinskas, M. Beresna, and P. G. Kazansky, *Appl. Phys. Lett.* **107**, 041114 (2015).
- ³⁶ X. Ji, L. Jiang, X. Li, W. Han, Y. Liu, Q. Huang, and Y. Lu, *Appl. Opt.* **53**, 6742 (2014).
- ³⁷ T. Schwarz-Selinger, D. G. Cahill, S.-C. Chen, S.-J. Moon, and C. P. Grigoropoulos, *Phys. Rev. B* **64**, 155323 (2001).
- ³⁸ S. R. Vatsya and S. K. Nikumb, *Phys. Rev. B* **68**, 035410 (2003).
- ³⁹ Y. Lu, S. Theppakuttai, and S. C. Chen, *Appl. Phys. Lett.* **82**, 4143 (2003).
- ⁴⁰ A. Ben-Yakar, A. Harkin, J. Ashmore, R. L. Byer, and H. A. Stone, *J. Phys. D: Appl. Phys.* **40**, 1447 (2007).
- ⁴¹ V. R. Bhardwaj, E. Simova, P. P. Rajeev, C. Hnatovsky, R. S. Taylor, D. M. Rayner, and P. B. Corkum, *Phys. Rev. Lett.* **96**, 057404 (2006).
- ⁴² P. P. Rajeev, M. Gertsvolf, C. Hnatovsky, E. Simova, R. S. Taylor, P. B. Corkum, D. M. Rayner, and V. R. Bhardwaj, *J. Phys. B* **40**, S273 (2007).
- ⁴³ J.-M. Guay, A. Villfranca, F. Baset, K. Popov, L. Ramunno, and V. R. Bhardwaj, *New J. Phys.* **14**, 085010 (2012).
- ⁴⁴ S. Ghimire, A. D. DiChiara, E. Sistrunk, P. Agostini, L. F. DiMauro, and D. A. Reis, *Nat. Phys.* **7**, 138 (2011).
- ⁴⁵ T. Luu, M. Garg, S. Y. Kruchinin, A. Moulet, M. T. Hassan, and E. Goulielmakis, *Nature* **521**, 498 (2015).
- ⁴⁶ O. Schubert *et al.*, *Nat. Photonics* **8**, 119 (2014).
- ⁴⁷ G. Vampa, T. J. Hammond, N. Thir, B. E. Schmidt, F. Lgar, D. D. Klug, and P. B. Corkum, e-print [arXiv:1605.06345](https://arxiv.org/abs/1605.06345) (2016).
- ⁴⁸ G. Vampa, B. G. Ghamsari, S. Siadat Mousavi, T. J. Hammond, A. Olivieri, E. Lisicka-Skrek, A. Yu Naumov, D. M. Villeneuve, A. Staudte, P. Berini, and P. B. Corkum, *Nat. Phys.* **13**, 659 (2017).
- ⁴⁹ M. Sivilis, M. Tauer, K. Johnston, G. Vampa, A. Staudte, A. Naumov, D. M. Villeneuve, C. Ropers, and P. B. Corkum *Science* **357**, 303 (2017).